

Experimental and Theoretical Density Functional Theory Approaches for Desulfurization of Dibenzothiophene from Diesel Fuel with Imidazole-Based Heteropolyacid Catalysts

Zhuoyi Ren, Qibin Yuan, Chunyan Dai, and Linhua Zhu*



Cite This: *ACS Omega* 2023, 8, 5593–5606



Read Online

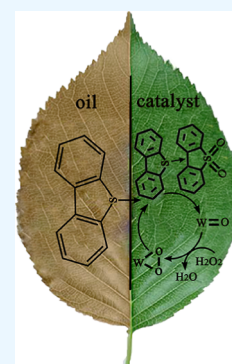
ACCESS |

Metrics & More

Article Recommendations

Supporting Information

ABSTRACT: Oxidative desulfurization (ODS) has been proved to be an efficient strategy for the removal of aromatic sulfur compounds from diesel oils, which are one of the main sources of air pollution. Heteropolyacid catalysts are highly active species for ODS, but the promotion of their catalytic activity and clarification of their catalytic mechanism remain an important issue. Herein, a series of novel imidazole-based heteropolyacid catalysts are prepared by a one-pot method for multiphase deep ODS of fuel with hydrogen peroxide as an oxidant. The experimental results show that the desulfurization performance of the prepared imidazole-based heteropolyacid catalysts is high up to 99.9% under mild conditions. The catalyst also possesses excellent recovery performance, and the desulfurization activity remains at 97.7% after being recycled seven times. Furthermore, density functional theory calculation is first employed to clarify the origin of the high desulfurization activity, and the results show that with the imidazole-based heteropolyacid (HPW-VIM) as the catalyst, the energy barrier is much lower than that with phosphotungstic acid (HPW) as the catalyst.



1. INTRODUCTION

The huge consumption of fossil fuels releases SO_x , leading to increasingly serious air pollution and some other environmental issues. Countries and regions around the world have launched increasingly strict regulations on sulfur contents in fuel oils. Therefore, reducing or even totally removing sulfur contents in fuel oils is an inevitable trend, which is also of great significance for improving the global environment and achieving sustainable development.^{1,2} At present, fuel desulfurization technology can be divided into two categories: hydrodesulfurization (HDS) and non-HDS. Among them, HDS needs to be carried out under high-temperature and high-pressure conditions, making the cost of HDS relatively high.^{3–5} Compared with other organic sulfur compounds, refractory sulfur (RS) compounds have larger steric hindrances and are more stable and difficult to remove in HDS.^{6,7} Under this circumstance, researchers have conducted a series of studies on non-HDS approaches such as biological desulfurization,^{8,9} extractive desulfurization,^{10–13} adsorptive desulfurization,^{14–18} oxidative desulfurization (ODS),^{19–21} etc. Among all these non-HDS methods, ODS has been proved to be an efficient one, in which organic sulfides are oxidized to sulfoxides or sulfones with higher polarities under mild conditions. Chen et al. obtained a polyoxometalate-based ionic liquid-supported three-dimensionally ordered macroporous silica structure material for heterogeneous ODS. The experimental results showed that the desulfurization efficiency of the catalyst remained to be 94% after the 14th cycle.²² In the ODS process, numerous oxidants including H_2O_2 ,^{23,24} oxygen,^{25–28} and *tert*-butyl hydroperoxide^{29,30} have been intensively employed. H_2O_2 has more active oxygen and only

produces water after the reaction, which has found extensive applications in ODS as an oxidant agent owing to its eco-sustainability.^{31,32}

Heteropolyacid (HPA) is an oxoacid with specific metal and non-metal composition. It has a high catalytic activity and stable structure and has been widely used in many oxidation systems in the past decades. In the ODS process, the removal efficiency of sulfide can be effectively improved by changing the structure of the HPAs.^{33,34} Ghubayra et al. proposed that the HPAs as those of Keggin loaded onto activated carbon to prepare the $\text{H}_3\text{PMo}_{12}\text{O}_{40}/\text{C}$ catalyst exhibited effective dibenzothiophene (DBT) removal efficiency under mild conditions.³⁵ Sulfated ionic liquids can be used as extractants and catalysts for extremely refractory thiophene. Bryzhin et al. mixed HPAs ($\text{H}_3\text{PMo}_{12}\text{O}_{40}$ or $\text{H}_3\text{PW}_{12}\text{O}_{40}$) with sulfated ionic liquids. The benzothiophene removal efficiency of the catalyst was 99.62% with an agitation rate of 300 rpm at a reaction temperature of 60 °C.³⁶ Rezvani and Miri first reported DBT transformation efficiency with Mn supported on Keggin-type $\text{H}_3\text{PW}_{12}\text{O}_{40}$ reaching 97% at 35 °C for 1 h.³⁷

1-Vinylimidazole (VIM) has low toxicity and biodegradability. Its double bond and imidazole group make it have many

Received: October 31, 2022

Accepted: January 20, 2023

Published: February 2, 2023



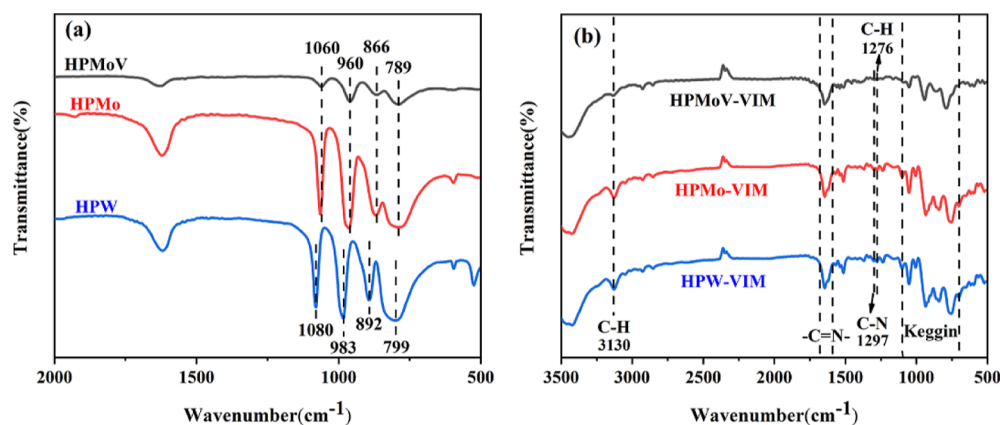


Figure 1. FT-IR spectra of (a) HPA and (b) HPA-VIM.

binding sites and play an important role in desulfurization.³⁸ To the best of our knowledge, only a few studies employed imidazole-based HPAs for the ODS process. Zhang et al. prepared imidazole-based phosphorus molybdenum vanadium ionic liquid by the anion exchange method, which achieved a 98.9% DBT conversion.³⁹ Butt et al. prepared a new type of ionic liquid with imidazole as the raw material through a three-step double alkylation and anion exchange reaction, thereby improving the desulfurization efficiency.⁴⁰ The catalytic performance of HPA is related to the width of the gap. Li et al. proved the important role of the close relationship between the HPAs modified by different metals and the ODS performance by density functional theory (DFT) calculation.⁴¹ Moreover, there is no systematic discussion on the mechanism of ODS by DFT.

In this study, we successfully prepared a series of VIM-based HPA catalysts with different HPA substitutions by the one-pot method and applied them to explore the catalytic performance in the ODS process. In addition, the reaction mechanism of the ODS process is proposed based on the experimental and analytical results.

2. EXPERIMENTAL SECTION

2.1. Materials and Characterizations. DBT (99%), phosphomolybdic acid hydrate (AR), molybdenum trioxide (AR, 99.5%), vanadium (V) oxide (99.99%), phosphoric acid (AR, purity ≥ 85 wt % in H_2O), and 1-methyl-3-octylimidazolium tetrafluoroborate (98%) were all purchased from Shanghai Macleans Biochemical Technology Co., Ltd. VIM (99%), phosphotungstic acid hydrate (AR), and tetradecane (AR, 99%) were received from Aladdin, China. Hydrogen peroxide (30 wt %) was purchased from Xilong Chemical Co., Ltd. Octane was obtained from Hushi Chemical Co., Ltd. All chemicals and reagents are used as direct receipts without further purification.

The Fourier-transform infrared (FT-IR) spectra of the prepared samples were obtained on a Nicolet 6700 intelligent Fourier infrared spectrometer (KBr pellets). The surface morphology of samples was measured using a JSM-7100F field-emission scanning electron microscope, and the samples were coated with platinum to improve the electrical conductivity. Powder X-ray diffraction (XRD) was performed using Ultima-IV, and the scanning rate was 2° min^{-1} in the 2θ range from 5 to 90° . A Thermo Scientific K-Alpha X-ray photoelectron spectrometer was used with the Al $K\alpha$ ray ($h\nu = 1486.6$ eV) as the excitation source to quantitatively analyze all elements

except H and He and determine the element valence in the material. Biod's high-performance specific surface and micro-pore analyzer Kubo-X1000 (BET) was used to characterize the catalysts. Thermogravimetric analysis (TGA) was performed on the STA 449 F3 Jupiter synchronous thermal analyzer; the temperature was 30 – 800°C , and the heating rate was $15^\circ\text{C} \cdot \text{min}^{-1}$. Cyclic voltammetry (CV) curves were tested in oxygen–nitrogen-saturated 0.1 M KOH solution using an electrochemical workstation (760E) from Shanghai Chenhua Instruments Co. Ltd. Detection of sulfide concentration changes in model oil was done by gas chromatography (GC) with the internal standard method (Agilent 7890; temperature program: 100°C ; temperature rising $15^\circ\text{C} \text{ min}^{-1}$; 250°C for 10 min; HP-5 MS column, $30 \text{ m} \times 250 \mu\text{m i.d.} \times 0.25 \mu\text{m}$). Analysis used the GC–mass spectrometry (MS) (Agilent 7890-5975; temperature program: 100°C ; heating $15^\circ\text{C} \text{ min}^{-1}$; 230°C incubation 10.2 min; HP-5 MS column, $30 \text{ m} \times 250 \mu\text{m i.d.} \times 0.25 \mu\text{m}$) product after the reaction.

2.2. Preparation of Imidazole-Based Heteropolyacid Catalysts. Novel imidazole-based HPAs were synthesized by the one-pot method. 1 mmol of $H_5PMo_{10}V_2O_{40}$ was dissolved in 40 mmol of VIM and mixed for 24 h at room temperature. A khaki–yellow precipitate appeared after stirring. The dispersion was filtered and washed with ethyl ether, repeatedly. Then, it was put in a vacuum drying oven at 40°C for 12 h. Finally, the synthesized sample was ground into powder, which was recorded as HPMoV-VIM. Simultaneously, other catalysts with different species of HPA were also prepared with a similar method and denoted HPMo-VIM and HPW-VIM. The detailed synthesis steps for HPMoV are shown in the Supporting Information.

2.3. ODS Process. The model oil is prepared by adding a certain amount of tetradecane (internal standard) and DBT (corresponding sulfur content is 500 ppm) to n -octane. The ODS performance was tested in a bottle set equipped with a magnetic stirrer, a condensate tube, and a constant temperature water bath. In a typical run, 50 mg of the catalyst and 5 mL of model oil were added to the reactor and then placed in a 50°C constant temperature water bath and stirred magnetically at 1000 rpm. Afterward, the time was recorded while adding the appropriate amount of ionic liquid (1 mL) and 30% hydrogen peroxide in turn. The sample was taken out at regular intervals and left for a while before sampling until the catalyst and the oil phase were completely separated. Finally, the obtained model oil was tested by GC to detect the remaining sulfur content at that time. After the reaction, the residual sulfur content was tested via

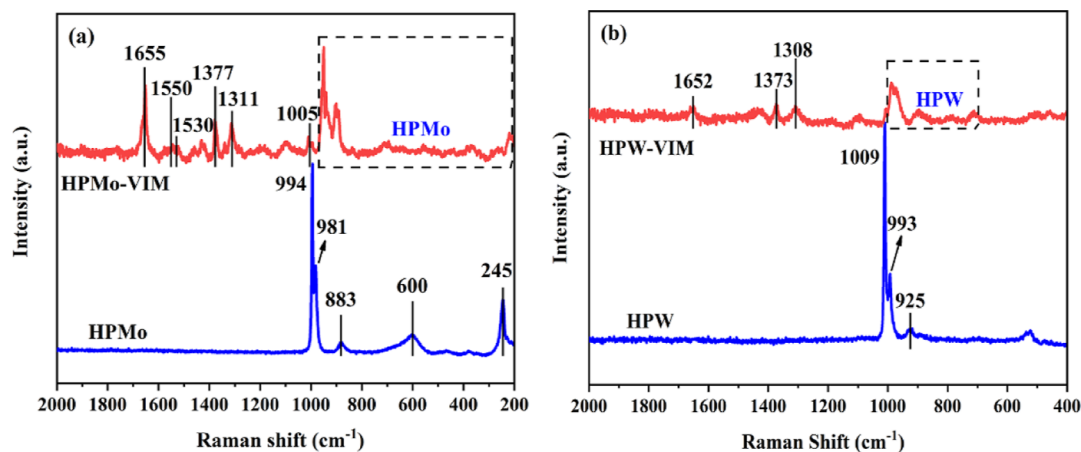


Figure 2. Raman spectrum of (a) HPMo-VIM and HPMo and (b) HPW-VIM and HPW.

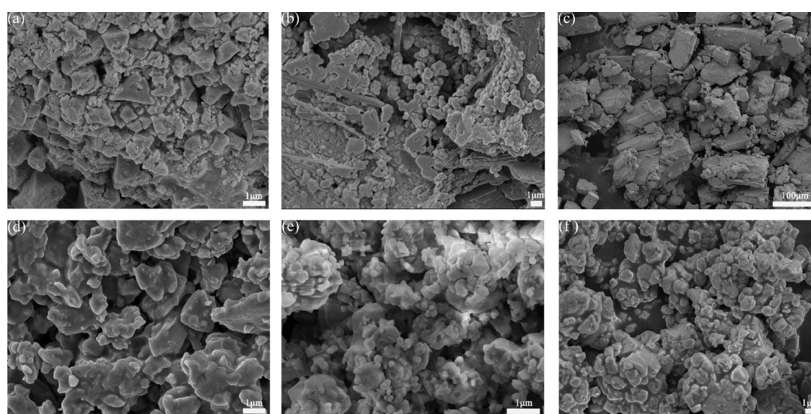


Figure 3. SEM images of (a) HPMoV; (b) HPMo; (c) HPW; (d) HPMoV-VIM; (e) HPMo-VIM; and (f) HPW-VIM.

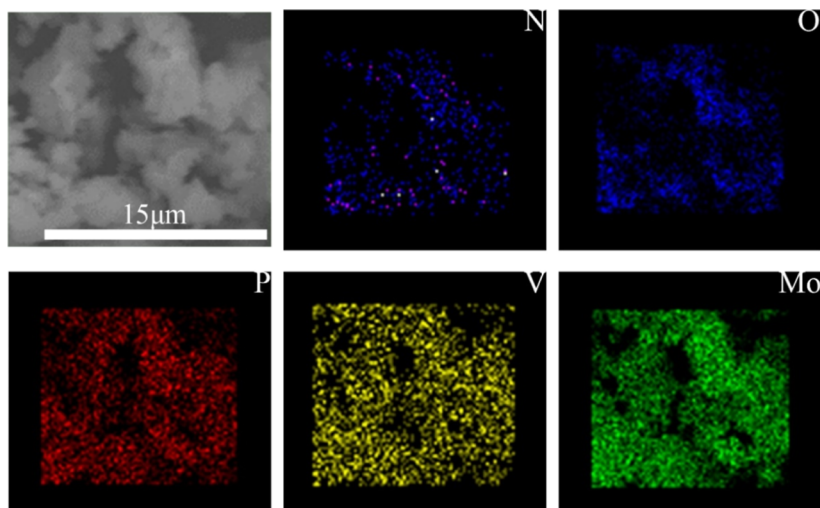


Figure 4. Elemental (C, N, O, P, V, and Mo) mapping of HPMoV-VIM.

an internal standard (tetradecane, 4000 ppm) method using a gas chromatograph equipped with a capillary column (HP-5, 30 m \times 0.25 mm \times 0.25 μ m). The injector temperature was 300 $^{\circ}$ C, and the detector temperature was 250 $^{\circ}$ C. The temperature of the GC process started at 100 $^{\circ}$ C and rose to 250 $^{\circ}$ C at 15 $^{\circ}$ C/min. The sulfur removal (%) was calculated using the following equation

$$\text{sulfur removal (\%)} = \frac{\text{initial sulfur content} - \text{residual sulfur content}}{\text{initial sulfur content}} \times 100\%$$

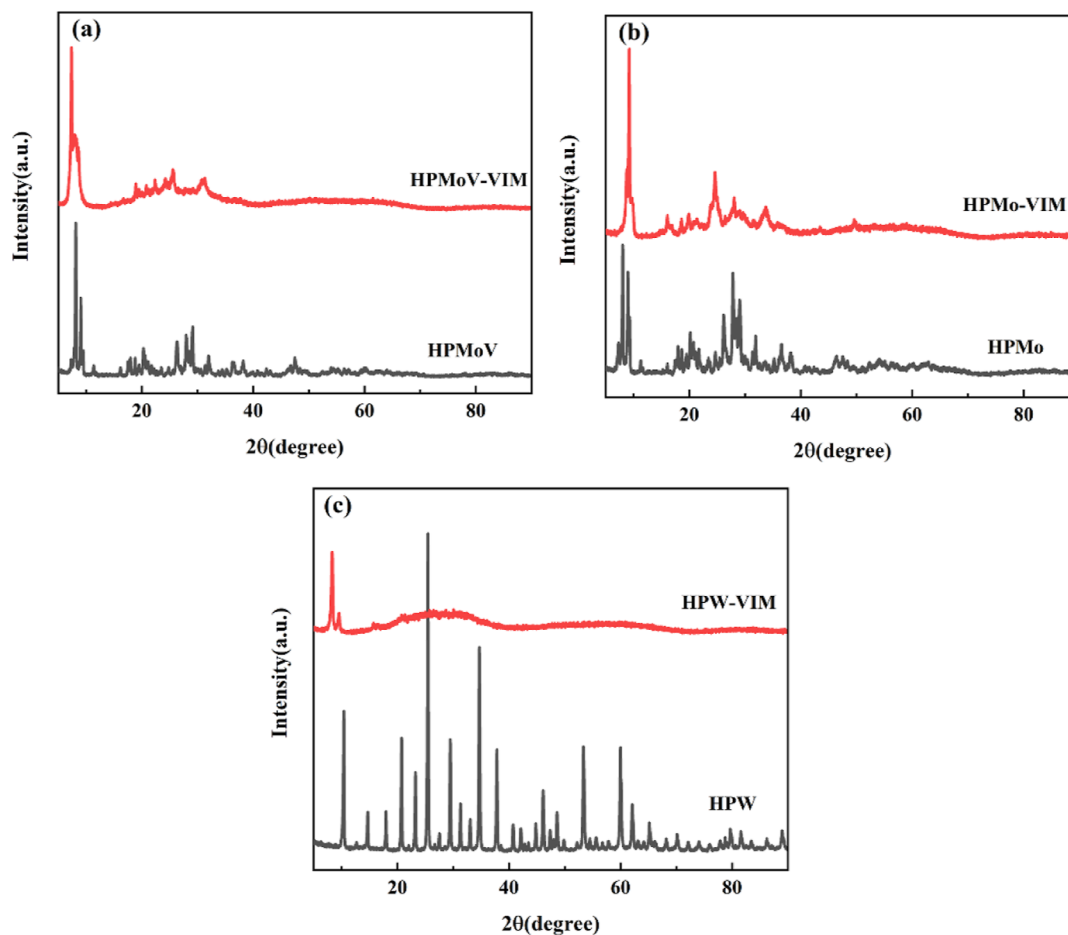


Figure 5. XRD patterns of various samples. (a) HPMoV-VIM and HPMoV, (b) HPMo-VIM and HPMo, and (c) HPW-VIM and HPW.



Figure 6. Contact angle on the surface of (a) HPMoV-VIM, (b) HPMo-VIM, and (c) HPW-VIM.

3. RESULTS AND DISCUSSION

3.1. Characterization of Catalysts. To ascertain the chemical bonds and functional groups of the catalysts, we carried out FT-IR analysis of phosphomolybdic vanadium HPA (HPMoV) and phosphomolybdic acid (HPMo), phosphotungstic acid (HPW), and their imidazole-based HPA (HPMoV-VIM, HPMo-VIM, and HPW-VIM). Figure 1a is the FT-IR spectra of HPMoV, HPMo, and HPW. The absorption bands of HPMoV are 1060 cm^{-1} (P–O), 960 cm^{-1} (Mo=O), 866 cm^{-1} (Mo–O–Mo corner-sharing), and 789 cm^{-1} (Mo–O–Mo edge-sharing), which are similar to those of HPMo.⁴² This result indicates the successful replacement of vanadium without changing the Keggin framework. Figure 1a also shows four characteristic absorption bands of the Keggin-type HPW at $1080, 983, 892,$ and 799 cm^{-1} . The peaks correspond to the vibrations of P–O_a, W–O_d, W–O_b–W, and W–O_c–W, respectively.⁴³ On the other hand, FT-IR spectra of the imidazole-based catalysts with different types of HPAs are also displayed in Figure 1b. A spectral band near 3130 cm^{-1} is attributed to the vibration of the unsaturated C–H

group, proving the existence of the vinyl group. The band at $1680\text{--}1590\text{ cm}^{-1}$ is ascribed to the stretching vibrations of –C=N– of the imidazole ring.^{44,45} 1276 and 1297 cm^{-1} are C–H (ring) in-plane bending vibration and C–N (ring) stretching vibration, respectively.⁴⁶ Besides, all samples also show four characteristic bands of the Keggin structure in the range of $700\text{--}1000\text{ cm}^{-1}$. The characteristic peaks of the Keggin-type structure on HPW-VIM shift slightly, indicating the existence of strong $\pi\text{--}\pi$ interaction between HPW and VIM.

Raman spectroscopy is a universal characterization method for identifying HPAs. The pure HPA and HPA-VIM catalysts were studied in Figure 2. For pure HPMo, some peaks at approximately $994, 981, 883, 600,$ and 245 cm^{-1} can be observed belonging to the symmetrical stretching vibration of Mo–O_d, asymmetric stretching vibration of Mo–O_d, asymmetric stretching vibration of Mo–O_b–Mo, asymmetric stretching vibration of Mo–O_c–Mo, and symmetrical stretching vibration of Mo–O_a, respectively (Figure 2a).⁴⁷ The ν (C=N) or ν (C=C), ν (C–H), ν (C–N), ν_s ring (C–N), ν_{as} ring (C–N), and δ ring of VIM are established at $1655, 1550, 1530, 1377, 1311,$ and

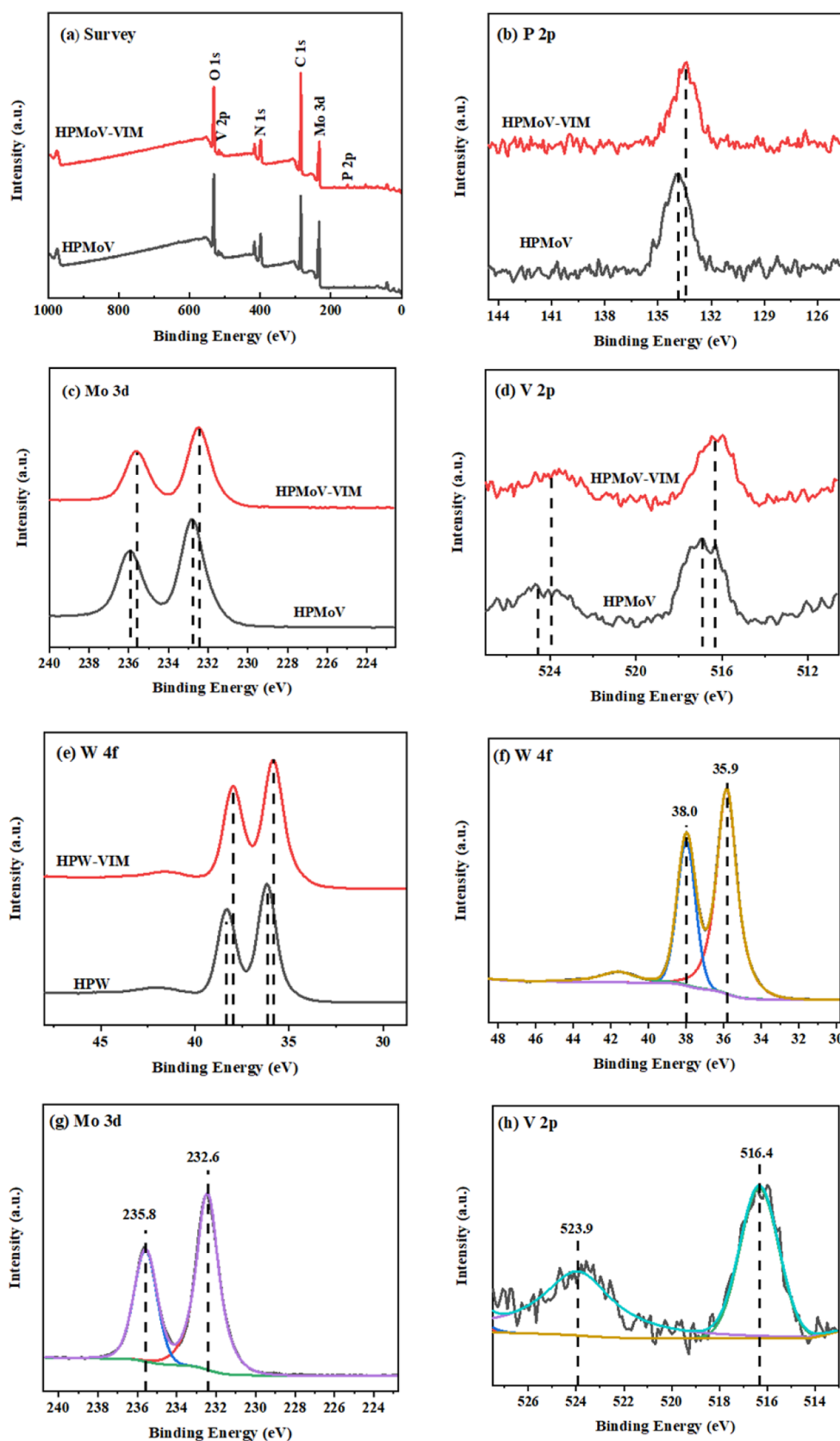


Figure 7. XPS spectra of (a) survey, (b) P 2p, (c) Mo 3d, and (d) V 2p of HPMoV-VIM; (e) W 4f of HPW-VIM; peak deconvolutions for (f) W 4f of HPW-VIM; and (g) Mo 3d and (h) V 2p of HPMoV-VIM.

1005 cm^{-1} as shown in Figure 2a, respectively.^{48,49} These characteristic bands of the Keggin structure were retained for

HPMoV-VIM catalysts as shown in Figure 2a. Three peaks of the pure HPW in the range of $1100\text{--}900\text{ cm}^{-1}$ are assigned to the

Table 1. ODS Performance of Different Catalysts^a

entry	samples	desulfurization rate (%)
1	without catalyst	2.1
2	HPW	28.76
3	HPMo	85.35
4	HPMoV	33.40
5	HPW-VIM	99.91
6	HPMo-VIM	95.18
7	HPMoV-VIM	86.20

^aReaction conditions: m (catalyst) = 0.05 g, T = 50 °C, t = 60 min, $V(\text{H}_2\text{O}_2)$ = 40 μL .

Keggin structure (Figure 2b), which are approximately 1009, 993, and 925 cm^{-1} and correspond to the symmetric stretching vibration of $\text{W}=\text{O}$, asymmetric stretching vibration of $\text{W}=\text{O}$, and the bridging vibration of $\text{W}-\text{O}_\text{b}-\text{W}$ bonds, respectively.^{50–53} Slight shifts occur for various samples due to the chemical interaction between HPA and the VIM surface. The Raman spectra of HPMoV and HPMoV-VIM are shown in Figure S1, where HPMoV and HPMo have similar characteristic peaks.

To more intuitively observe the morphology of samples, an effort was made to examine the catalysts using scanning electron microscopy (SEM). As seen in Figure 3, compared with the pure HPA with a blocky structure (Figure 3a–c), HPMoV-VIM, HPMo-VIM, and HPW-VIM (Figure 3d–f) are less agglomerated. They are evenly distributed, which is beneficial for the catalytic reaction compared to bulk HPAs. The elemental

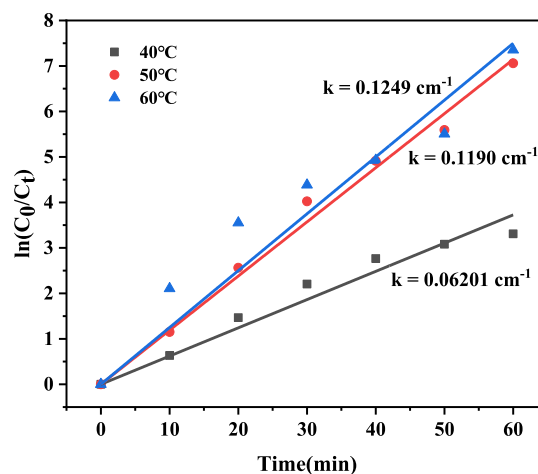


Figure 9. Pseudo-first-order kinetics for the oxidation of DBT at different reaction temperatures in the ODS system. Experimental conditions: m (catalyst) = 0.05 g, O/S = 5, $V(\text{model oil})$ = 5 mL.

composition of HPMoV-VIM is determined in the element mapping image (Figure 4). It also further confirms that the N, O, P, V, and Mo elements are evenly dispersed throughout the catalyst. In addition, the element mapping diagrams of other catalysts are shown in Figures S2–S6. Elements and diagrams correspond to each other, proving that the elements are evenly distributed (Figures S2–S6, Supporting Information).

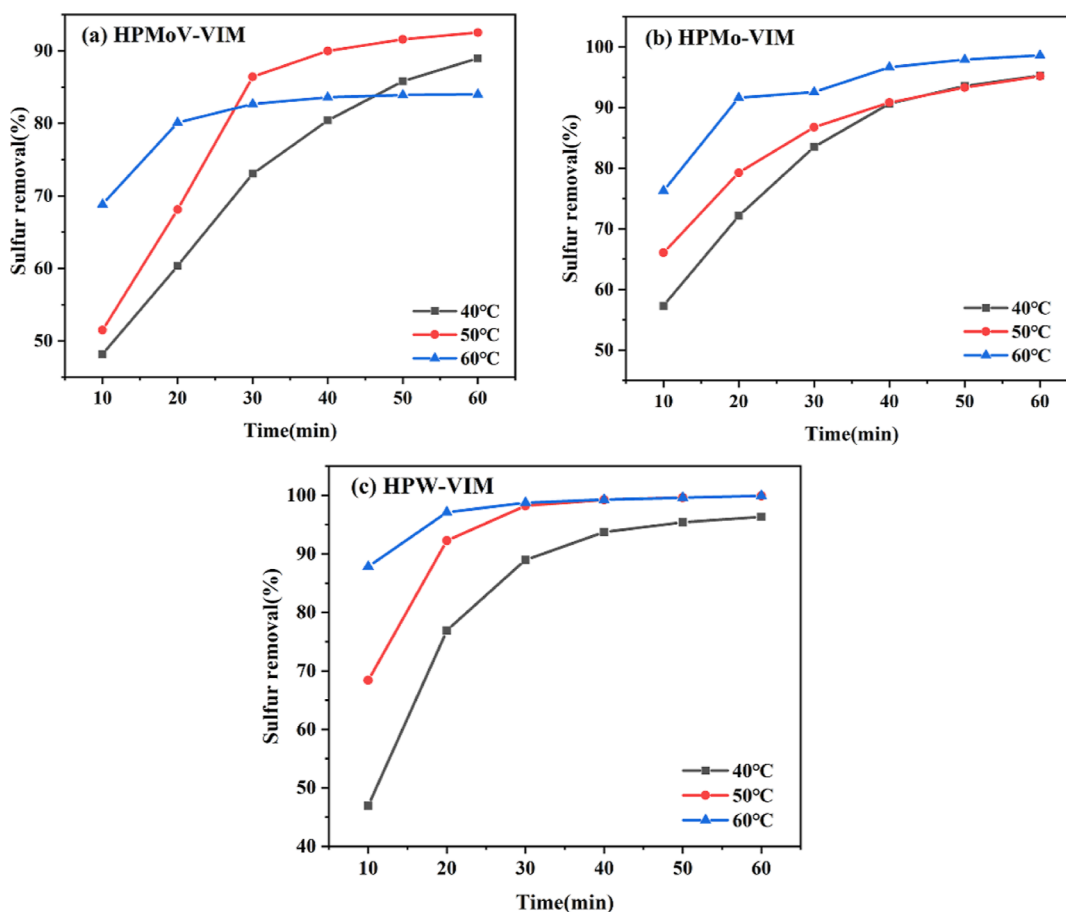


Figure 8. Effect of different temperatures on ODS. Reaction condition: m (catalyst) = 0.05 g, O/S = 5, $V(\text{model oil})$ = 5 mL.

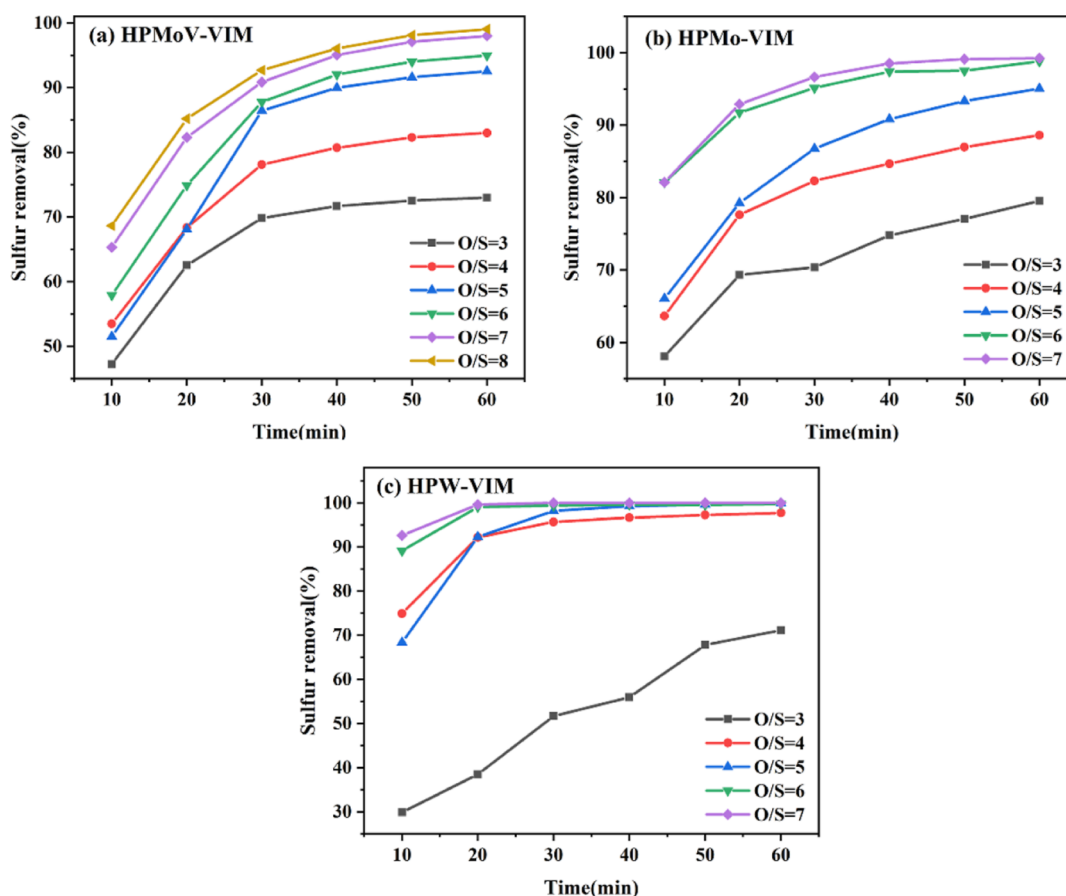


Figure 10. Effect of different oxygen–sulfur ratios on ODS. Reaction condition: $m(\text{catalyst}) = 0.05 \text{ g}$, $T = 50 \text{ }^\circ\text{C}$, $V(\text{model oil}) = 5 \text{ mL}$.

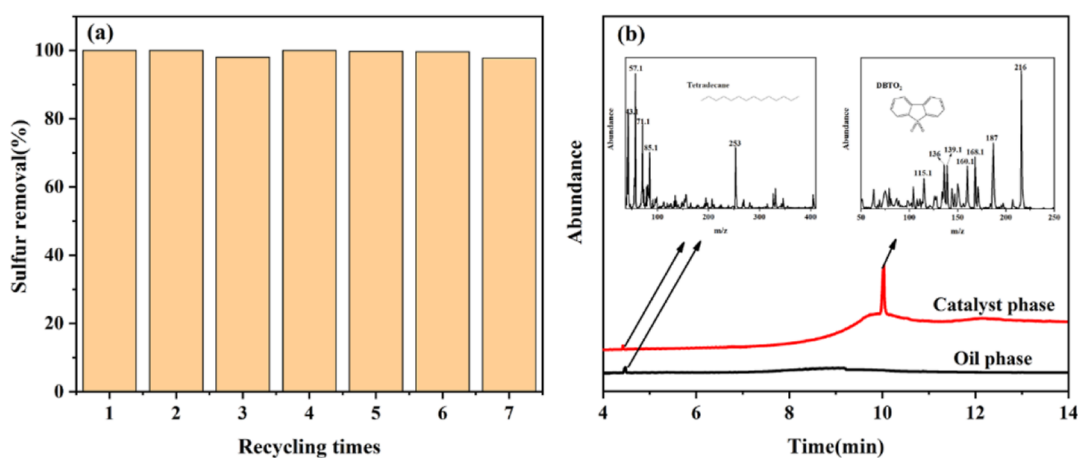


Figure 11. (a) Cycling performance of catalysts and (b) GC–MS analysis of the catalyst phase and oil phase after the reaction.

The crystal structure of the prepared samples was further studied by XRD. The XRD patterns of the catalysts are depicted in Figure 5. According to literature reports, the characteristic diffraction of the Keggin structure of HPMoV is located at $2\theta = 7\text{--}9$, $15\text{--}22$, and $25\text{--}28^\circ$ (Figure 5a).⁵⁴ For HPMo, characteristic structures appear at $7\text{--}12$, $15\text{--}22$, and $26\text{--}30^\circ$. The observed peaks of the Keggin-type crystal lay in the range of $2\theta = 5\text{--}35^\circ$ (Figure 5b).⁵⁵ It could be observed that the Keggin structure of the HPA is retained after the introduction of imidazole (Figure 5a,b). The characteristic peak of HPW is not detected in HPW-VIM (Figure 5c). This phenomenon indicates the loss of crystal order, which is mainly due to the

rearrangement of HPW and VIM during the reaction process.⁵⁶ Another possible reason is that HPW is highly dispersed in the system.

Hydrophilicity and hydrophobicity play an important role in activating H_2O_2 in the ODS system. Figure 6 shows the contact angle analysis of different catalysts in the water phase. When the water droplets are added to the surface of the catalyst, they are wetted instantly. Compared with that of HPMoV-VIM (Figure 6a) and HPMo-VIM (Figure 6b), the contact angle of HPW-VIM (Figure 6c) is 7.7° , and it has better hydrophilicity. This allows the catalyst to contact the hydrogen peroxide better during the reaction process, thereby improving desulfurization

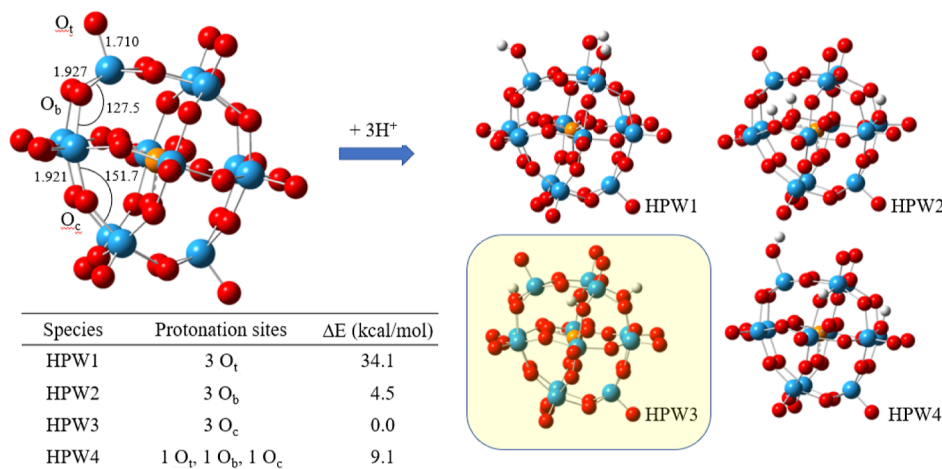


Figure 12. Optimized structure and the possible coordination sites of $\text{PW}_{12}\text{O}_{40}^{3-}$.

efficiency.⁵⁷ The contact angles of HPMoV, HPMo, and HPW are shown in Figure S7 (Figure S7, Supporting Information).

To analyze the composition of the catalyst and the chemical state of its elements, we further qualitatively analyzed the synthesized HPAs and the corresponding catalysts by XPS as shown in Figure 7. Figure 7a shows the survey spectrum of HPMoV and HPMoV-VIM. It can be seen that the HPMoV-VIM catalyst is composed of six elements: C, N, O, P, Mo, and V, which proves the successful reaction of HPMoV with VIM (Figure 7b–e). In addition, compared with those of the original HPA, the XPS peaks of the four elements P, Mo, V, and W in the catalyst all shift to lower binding energies after the addition of imidazole, indicating that electron transfer occurred during the reaction, which also proves that the sample was successfully synthesized. After this, we fit the peaks of metal elements. It can be seen from Figure 7f that the two peaks appearing at the binding energies of 38.0 and 35.9 eV are attributed to W $4f_{5/2}$ and W $5f_{7/2}$, respectively, indicating that the element in the catalyst is W^{6+} .⁵⁸ As shown in Figure 7g, the peaks at 235.8 and 232.6 eV correspond to Mo $3d_{5/2}$ and Mo $3d_{3/2}$, respectively. The difference in binding energy between Mo $3d_{5/2}$ and Mo $3d_{3/2}$ is 3.2 eV.⁵⁹ The peaks at 523.9 and 516.4 eV shown in Figure 7h correspond to V $2p_{1/2}$ and V $2p_{3/2}$, respectively. Also, the peak intensity of V $2p_{3/2}$ is higher than that of V $2p_{1/2}$.^{60,61} The above-mentioned results indicate that the valence states of the metal elements W, Mo, and V did not change, and the imidazole-based HPAs were successfully synthesized during the reaction. The survey XPS analysis chart of each catalyst is shown in Figure S8. The binding energy peaks of N, O, P, Mo, or W can be found, indicating the successful synthesis of the catalysts (Figure S8, Supporting Information).

3.2. Catalytic Performance. Table 1 shows the desulfurization efficiency of different catalysts under the same conditions. The low efficiency of the three different HPAs may be due to the large particle size of the materials making it difficult to fully contact and react with the sulfides in the oil. The desulfurization efficiency of the imidazole-based HPAs can reach 99.91, 95.18, and 86.20%, respectively, under the same conditions, showing excellent catalytic oxidation desulfurization performance, and the order of activity is HPW-VIM > HPMo-VIM > HPMoV-VIM. These results suggest that imidazole-based HPAs play important roles in the ODS process.

Temperature is an important factor affecting desulfurization performance. The higher the temperature, the faster the speed of

molecular motion. The removal effect of DBT is better (Figure 8b,c). The desulfurization experiment found that when the temperature increased from 40 to 50 °C, the decomposition rate of hydrogen peroxide increased, which achieved the purpose of deep desulfurization (Figure 8). When the temperature rose to 60 °C, the desulfurization rate did not increase but decreased instead. This is because the decomposition rate of hydrogen peroxide is too fast, and the oxygen atoms are not fully utilized for desulfurization.

By comparing the turnover frequency (TOF) values of different catalysts, we can objectively compare their activity. The TOF was calculated and is summarized in Table S1. It can be seen that the TOF value of the HPW-VIM catalyst was higher than that of the other catalysts.

For a better exploration of the relationship between desulfurization efficiency and temperature, we investigated the desulfurization kinetics at different reaction temperatures. Figure 9 shows the relationship between $\ln(C_0/C_t)$ and reaction time of HPW-VIM at different temperatures. As can be seen in Figure 9, the rate constants k of the desulfurization reaction at 40, 50, and 60 °C are, respectively, 0.0621, 0.1190, and 0.1249, which conform to the pseudo-first-order kinetic equation. It was further confirmed that the rate of the ODS reaction increased with the increase in temperature. The Arrhenius equation is the empirical formula for the relationship between the chemical reaction rate constant and temperature (eq 1). By deriving the Arrhenius equation, the relationship between curing temperature and curing time can be obtained in eq 2. Furthermore, the apparent activation energy of DBT oxidation with the HPW-VIM catalyst is 30.3 $\text{kJ}\cdot\text{mol}^{-1}$. The relationship between $\ln(C_0/C_t)$ of the HPW-VIM catalyst and reaction time at different oxygen–sulfur ratios is shown in Figure S9. The relationship between $\ln(C_0/C_t)$ and reaction time of different catalysts is shown in Figure S10, which identifies that the catalyst of HPW-VIM has the best effect in removing DBT.

$$k = A e^{-E_a/RT} \quad (1)$$

$$\ln \frac{k_2}{k_1} = \frac{E_a}{R} \left(\frac{1}{T_1} - \frac{1}{T_2} \right) \quad (2)$$

Under certain reaction conditions, we explored the effect of the amount of H_2O_2 on the desulfurization efficiency (Figure 10). Taking Figure 10c as an example, the desulfurization efficiency increases with the oxygen–sulfur rate. With the

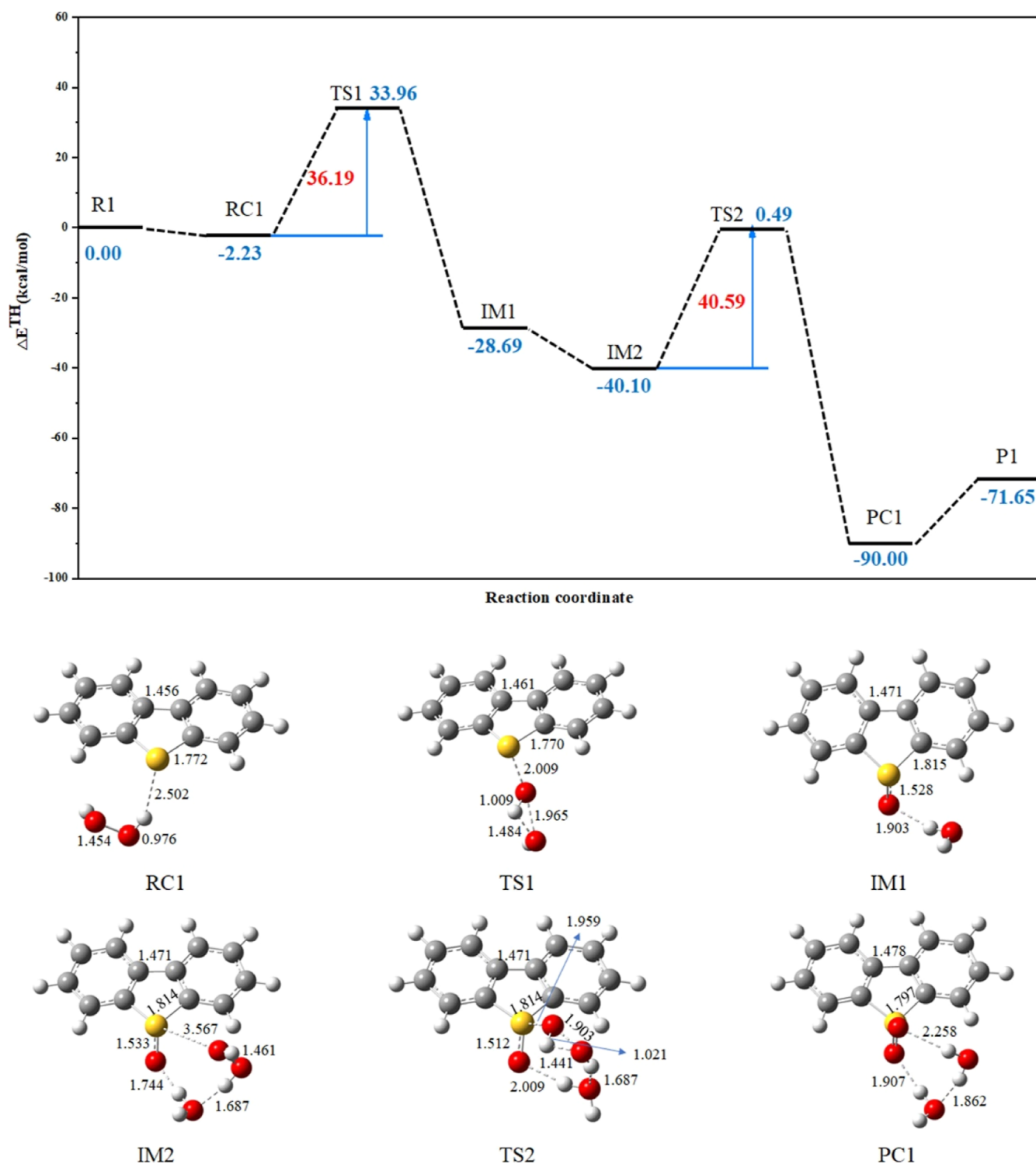


Figure 13. Potential energy distribution without the catalyst during ODS calculated by DFT.

increase in reaction time, the sulfur removal increased continuously as well. Sulfur removal reached 100% within 30 min when O/S increased to 5. In order to save resources, in the system with the HPW-VIM catalyst, an O/S of 5 is appropriate.

The stability of the catalyst is another important factor in the desulfurization system (Figure 11). The cycle performance is an important criterion for investigating the pros and cons of the catalyst, and it determines the prospect of the catalyst in industrial application. We took HPW-VIM as an example to

further test its reuse efficiency. The recovery performance of HPW-VIM is shown in Figure 11a. After the ODS, the upper oil phase was separated from the catalyst phase by decantation, and then, the catalyst phase in the reactor was transferred to a vacuum drying box and dried at 70 °C for 4 h. Then, fresh simulated oil was added to the reactor for the next experiment. After seven times recovery, the removal rate of sulfur can still reach 97.7%. Compared with that of the new HPW-VIM, the efficiency of HPW-VIM after seven cycles is only reduced by

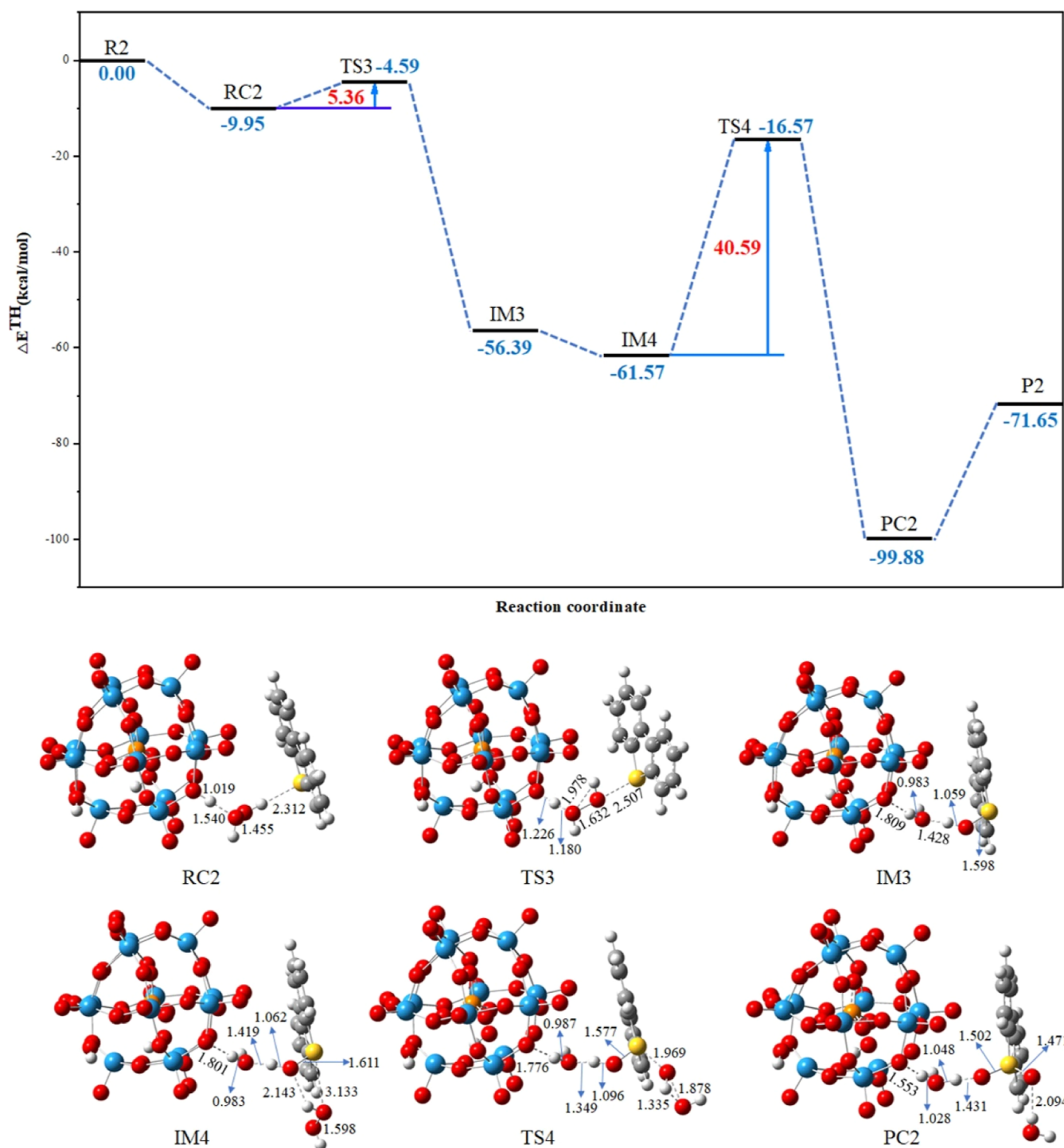


Figure 14. The potential energy distribution of HPW as a catalyst in the ODS process is calculated by DFT.

0.3%, indicating that the prepared samples have good recovery ability. We further confirmed the oxidation products with the oil and catalyst phases after the reaction by GC–MS analysis (Figure 11b). We find that the oil phase and the catalyst phase have the same peak at about 4.5 min, which is the characteristic peak of tetradecane. In the oil phase, DBT has no obvious peak, indicating that the degree of DBT degradation is high. A peak corresponding to sulfone (DBTO₂) appears in the catalyst phase at around 10.1 min, indicating that DBT is oxidized to DBTO₂.

3.3. Proposed Mechanism. As mentioned above, the HPW-VIM catalyst plays an important role in the ODS reaction.

To further understand the function of HPW and HPW-VIM in the ODS process, DFT calculations are employed to clarify the mechanism. Using the hybrid functional of B3LYP, the 6-31G(d,p) basis set is selected to optimize H, C, N, O, and S elements. Since the W element is after the third cycle, we choose the LANL2DZ basis set for optimization.

The fully optimized structure and the possible coordination sites of the key species PW₁₂O₄₀³⁻ are presented in Figure 12, whereas Figures 13–15 show the calculated potential energy profiles for the ODS process. It can be seen from the calculation that when combined with Oc, the required energy is 0, and the

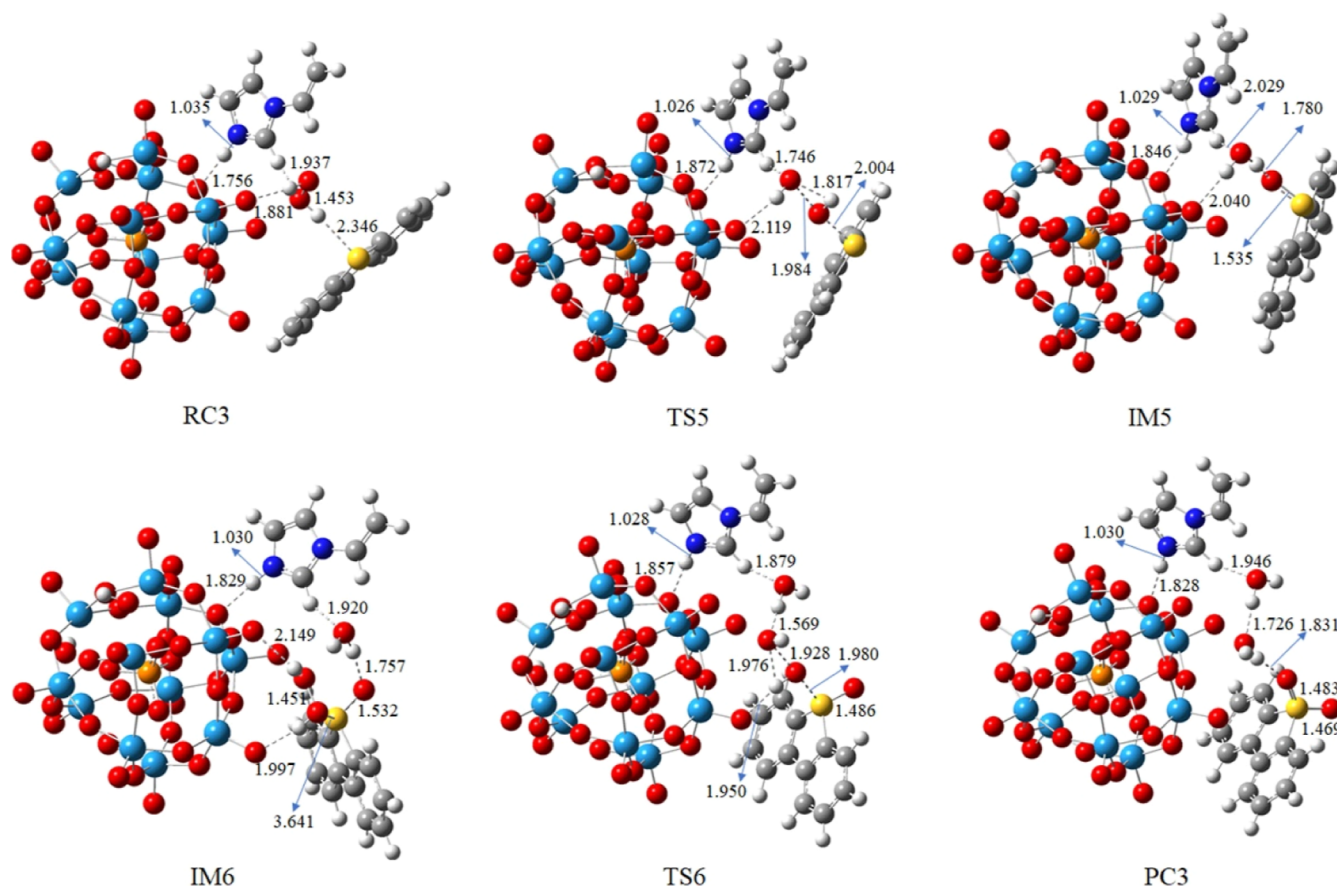
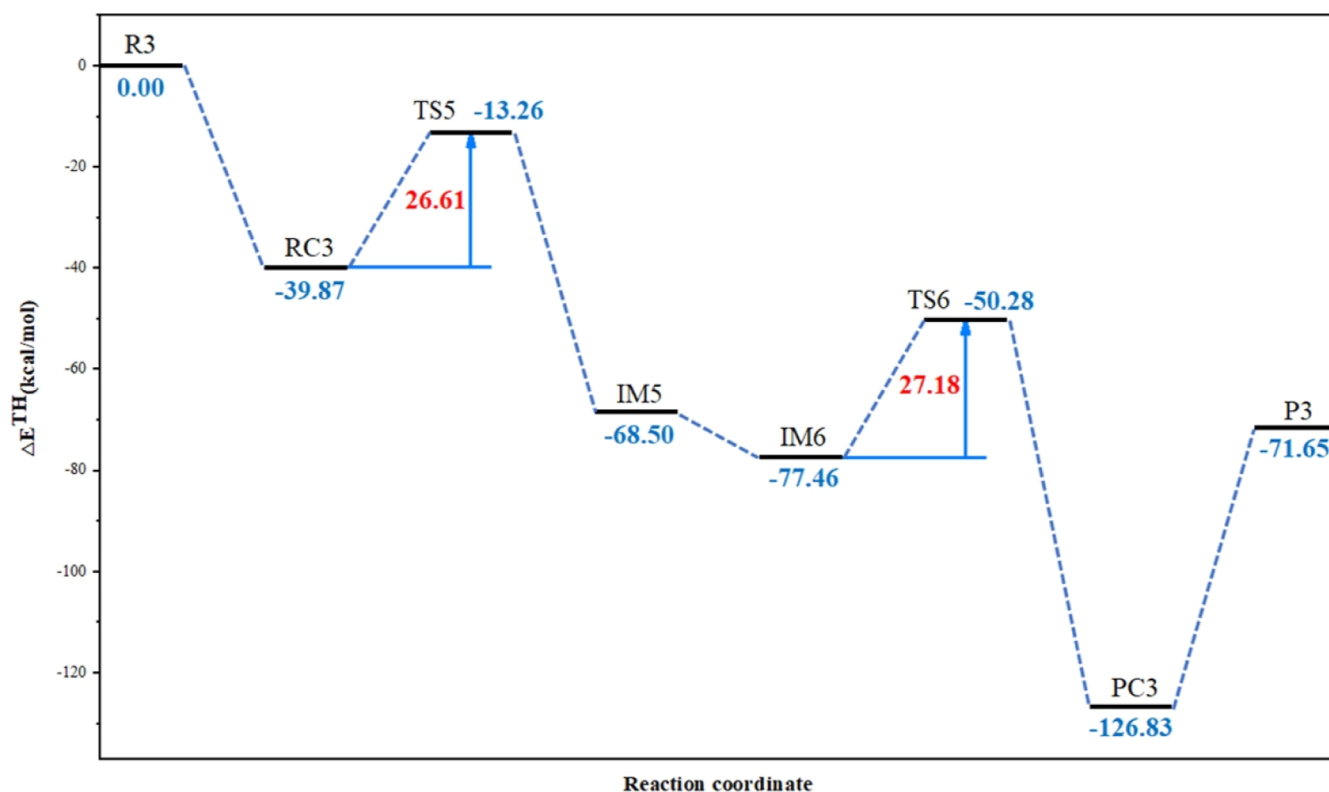


Figure 15. The potential energy distribution of HPW-VIM as a catalyst in the ODS process is calculated by DFT.

structure is relatively stable.^{18,62} Figure 13 shows the calculated energy profile of the proposed DBT oxidation reaction mechanism without a catalyst. Also, the activation energy

barriers for the two steps are 36.2 and 40.6 kcal/mol, respectively. In the presence of an HPW catalyst, the activation energy barriers for the first step are quite low (5.4 kcal/mol) but

Notes

The authors declare no competing financial interest.

ACKNOWLEDGMENTS

The authors thank Guangying Chen and Hongping Li for help and support in DFT. This work was supported by the Innovative Research Team Project of the Hainan Natural Science Foundation (220CXTD436) and Key Research and Development Plan of Hainan Province (ZDYF2022SHFZ285).

REFERENCES

- (1) Shi, X.; Zheng, Y.; Lei, Y.; Xue, W.; Yan, G.; Liu, X.; Cai, B.; Tong, D.; Wang, J. Air quality benefits of achieving carbon neutrality in China. *Sci. Total Environ.* **2021**, *795*, 148784.
- (2) Li, X.; Zhang, J.; Zhou, F.; Wang, Y.; Yuan, X.; Wang, H. Oxidative desulfurization of dibenzothiophene and diesel by hydrogen peroxide: Catalysis of $\text{H}_3\text{PMo}_{12}\text{O}_{40}$ immobilized on the ionic liquid modified SiO_2 . *Mol. Catal.* **2018**, *452*, 93–99.
- (3) Bodin, A.; Christoffersen, A. N.; Elkjær, C. F.; Brorson, M.; Kibsgaard, J.; Helveg, S.; Chorkendorff, I. Engineering Ni-Mo-S Nanoparticles for Hydrodesulfurization. *Nano Lett.* **2018**, *18*, 3454–3460.
- (4) Wu, G.; Yin, Y.; Chen, W.; Xin, F.; Lu, Y.; Qin, K.; Zhang, L.; Song, Y.; Li, M. Catalytic kinetics for ultra-deep hydrodesulfurization of diesel. *Chem. Eng. Sci.* **2020**, *214*, 115446.
- (5) Liu, Z.; Han, W.; Hu, D.; Nie, H.; Wang, Z.; Sun, S.; Deng, Z.; Yang, Q. Promoting effects of SO_4^{2-} on a NiMo/ γ - Al_2O_3 hydrodesulfurization catalyst. *Catal. Sci. Technol.* **2020**, *10*, 5218–5230.
- (6) Liu, F.; Yu, J.; Qazi, A. B.; Zhang, L.; Liu, X. Metal-Based Ionic Liquids in Oxidative Desulfurization: A Critical Review. *Environ. Sci. Technol.* **2021**, *55*, 1419–1435.
- (7) Zou, J.; Lin, Y.; Wu, S.; Zhong, Y.; Yang, C. Molybdenum Dioxide Nanoparticles Anchored on Nitrogen-Doped Carbon Nanotubes as Oxidative Desulfurization Catalysts: Role of Electron Transfer in Activity and Reusability. *Adv. Funct. Mater.* **2021**, *31*, 2100442.
- (8) González-Cortés, J. J.; Torres-Herrera, S.; Almenglo, F.; Ramírez, M.; Cantero, D. Anoxic biogas biodesulfurization promoting elemental sulfur production in a continuous Stirred Tank Bioreactor. *J. Hazard. Mater.* **2021**, *401*, 123785.
- (9) Li, W.; Zhang, M.; Kang, D.; Chen, W.; Yu, T.; Xu, D.; Zeng, Z.; Li, Y.; Zheng, P. Mechanisms of sulfur selection and sulfur secretion in a biological sulfide removal (BISURE) system. *Environ. Int.* **2020**, *137*, 105549.
- (10) Rezaee, M.; Feyzi, F.; Dehghani, M. R. Extractive desulfurization of dibenzothiophene from normal octane using deep eutectic solvents as extracting agent. *J. Mol. Liq.* **2021**, *333*, 115991.
- (11) Player, L. C.; Chan, B.; Lui, M. Y.; Masters, A. F.; Maschmeyer, T. Toward an Understanding of the Forces Behind Extractive Desulfurization of Fuels with Ionic Liquids. *ACS Sustainable Chem. Eng.* **2019**, *7*, 4087–4093.
- (12) El-hoshoudy, A. N.; Soliman, F. S.; Abd El-Aty, D. M. Extractive desulfurization using choline chloride-based DES/molybdate nano-fluids; Experimental and theoretical investigation. *J. Mol. Liq.* **2020**, *318*, 114307.
- (13) Jiang, W.; Zhu, K.; Li, H.; Zhu, L.; Hua, M.; Xiao, J.; Wang, C.; Yang, Z.; Chen, G.; Zhu, W.; et al. Synergistic effect of dual Brønsted acidic deep eutectic solvents for oxidative desulfurization of diesel fuel. *Chem. Eng. J.* **2020**, *394*, 124831.
- (14) Zhu, H.; Li, X.; Shi, N.; Ding, X.; Yu, Z.; Zhao, W.; Ren, H.; Pan, Y.; Liu, Y.; Guo, W. Density functional theory study of thiophene desulfurization and conversion of desulfurization products on the Ni(111) surface and Ni_{55} cluster: implication for the mechanism of reactive adsorption desulfurization over Ni/ZnO catalysts. *Catal. Sci. Technol.* **2021**, *11*, 1615–1625.
- (15) Hasheminejad, N.; Tavakol, H.; Salvenmoser, W. Preparation of gold-decorated simple and sulfur-doped carbon spheres for desulfurization of fuel. *J. Cleaner Prod.* **2020**, *264*, 121684.
- (16) Sun, Y.; Li, L.; Ju, F.; Ling, H. Evolution of nickel species in reactive adsorption desulfurization of benzothiophene. *Sep. Purif. Technol.* **2022**, *283*, 120204.
- (17) Luo, J.; Wang, C.; Liu, J.; Wei, Y.; Chao, Y.; Zou, Y.; Mu, L.; Huang, Y.; Li, H.; Zhu, W. High-performance adsorptive desulfurization by ternary hybrid boron carbon nitride aerogel. *AIChE J.* **2021**, *67*, No. e17280.
- (18) Li, H.; Zhang, Y.; Lv, N.; Yin, J.; Zhang, J.; Ran, H.; Zhang, M.; Jiang, W.; Zhu, W.; Li, H. Unraveling the effects of O-doping into h-BN on the adsorptive desulfurization performance by DFT calculations. *J. Environ. Chem. Eng.* **2021**, *9*, 106463.
- (19) Zhu, W.; Li, H.; Jiang, X.; Yan, Y.; Lu, J.; He, L.; Xia, J. Commercially available molybdenic compound-catalyzed ultra-deep desulfurization of fuels in ionic liquids. *Green Chem.* **2008**, *10*, 641–646.
- (20) Jiang, Z.; Lü, H.; Zhang, Y.; Li, C. Oxidative Desulfurization of Fuel Oils. *Chin. J. Catal.* **2011**, *32*, 707–715.
- (21) Jiang, W.; Xiao, J.; Gao, X.; An, X.; Leng, Y.; Zhu, L.; Zhu, W.; Li, H. In situ fabrication of hollow silica confined defective molybdenum oxide for enhanced catalytic oxidative desulfurization of diesel fuels. *Fuel* **2021**, *305*, 121470.
- (22) Chen, X.; Zhang, M.; Wei, Y.; Li, H.; Liu, J.; Zhang, Q.; Zhu, W.; Li, H. Ionic liquid-supported 3DOM silica for efficient heterogeneous oxidative desulfurization. *Inorg. Chem. Front.* **2018**, *5*, 2478–2485.
- (23) Ding, W.; Zhu, W.; Xiong, J.; Yang, L.; Wei, A.; Zhang, M.; Li, H. Novel heterogeneous iron-based redox ionic liquid supported on SBA-15 for deep oxidative desulfurization of fuels. *Chem. Eng. J.* **2015**, *266*, 213–221.
- (24) Taghiyar, H.; Yadollahi, B. Keggin polyoxometalates encapsulated in molybdenum-iron-type Keplerate nanoball as efficient and cost-effective catalysts in the oxidative desulfurization of sulfides. *Sci. Total Environ.* **2020**, *708*, 134860.
- (25) Hao, L.; Stoian, S. A.; Weddle, L. R.; Zhang, Q. Zr-Based MOFs for oxidative desulfurization: What matters? *Green Chem.* **2020**, *22*, 6351–6356.
- (26) Sun, L.; Su, T.; Xu, J.; Hao, D.; Liao, W.; Zhao, Y.; Ren, W.; Deng, C.; Lü, H. Aerobic oxidative desulfurization coupling of Co polyanion catalysts and p-TsOH-based deep eutectic solvents through a biomimetic approach. *Green Chem.* **2019**, *21*, 2629–2634.
- (27) Wang, C.; Jiang, W.; Chen, H.; Zhu, L.; Luo, J.; Yang, W.; Chen, G.; Chen, Z.; Zhu, W.; Li, H. Pt nanoparticles encapsulated on V_2O_5 nanosheets carriers as efficient catalysts for promoted aerobic oxidative desulfurization performance. *Chin. J. Catal.* **2021**, *42*, 557–562.
- (28) Wang, C.; Daimon, H.; Onodera, T.; Koda, T.; Sun, S. A General Approach to the Size- and Shape-Controlled Synthesis of Platinum Nanoparticles and Their Catalytic Reduction of Oxygen. *Angew. Chem.* **2008**, *120*, 3644–3647.
- (29) Liu, Y.-Y.; Leus, K.; Sun, Z.; Li, X.; Depauw, H.; Wang, A.; Zhang, J.; Van Der Voort, P. Catalytic oxidative desulfurization of model and real diesel over a molybdenum anchored metal-organic framework. *Microporous Mesoporous Mater.* **2019**, *277*, 245–252.
- (30) Chen, L.; Ren, J.-T.; Yuan, Z.-Y. Atomic heterojunction-induced electron interaction in P-doped g- C_3N_4 nanosheets supported V-based nanocomposites for enhanced oxidative desulfurization. *Chem. Eng. J.* **2020**, *387*, 124164.
- (31) Rajendran, A.; Cui, T.-y.; Fan, H.-x.; Yang, Z.-f.; Feng, J.; Li, W.-y. A comprehensive review on oxidative desulfurization catalysts targeting clean energy and environment. *J. Mater. Chem. A* **2020**, *8*, 2246–2285.
- (32) Abazari, R.; Esrafil, L.; Morsali, A.; Wu, Y.; Gao, J. PMo_{12} @UiO-67 nanocomposite as a novel non-leaching catalyst with enhanced performance durability for sulfur removal from liquid fuels with exceptionally diluted oxidant. *Appl. Catal., B* **2021**, *283*, 119582.
- (33) Li, J.; Yang, Z.; Li, S.; Jin, Q.; Zhao, J. Review on oxidative desulfurization of fuel by supported heteropolyacid catalysts. *J. Ind. Eng. Chem.* **2020**, *82*, 1–16.
- (34) Taghizadeh, M.; Mehrvarz, E.; Taghipour, A. Polyoxometalate as an effective catalyst for the oxidative desulfurization of liquid fuels: a critical review. *Rev. Chem. Eng.* **2020**, *36*, 831–858.

- (35) Ghubayra, R.; Nuttall, C.; Hodgkiss, S.; Craven, M.; Kozhevnikova, E. F.; Kozhevnikov, I. V. Oxidative desulfurization of model diesel fuel catalyzed by carbon-supported heteropoly acids. *Appl. Catal., B* **2019**, *253*, 309–316.
- (36) Bryzhin, A. A.; Gantman, M. G.; Buryak, A. K.; Tarkhanova, I. G. Brønsted acidic SILP-based catalysts with $H_3PMo_{12}O_{40}$ or $H_3PW_{12}O_{40}$ in the oxidative desulfurization of fuels. *Appl. Catal., B* **2019**, *257*, 117938.
- (37) Rezvani, M. A.; Miri, O. F. Synthesis and characterization of PWMn/NiO/PAN nanosphere composite with superior catalytic activity for oxidative desulfurization of real fuel. *Chem. Eng. J.* **2019**, *369*, 775–783.
- (38) Ghandi, K. A Review of Ionic Liquids, Their Limits and Applications. *Green Sustainable Chem.* **2014**, *04*, 44–53.
- (39) Zhang, M.; Liu, J.; Li, H.; Wei, Y.; Fu, Y.; Liao, W.; Zhu, L.; Chen, G.; Zhu, W.; Li, H. Tuning the electrophilicity of vanadium-substituted polyoxometalate based ionic liquids for high-efficiency aerobic oxidative desulfurization. *Appl. Catal., B* **2020**, *271*, 118936.
- (40) Butt, H. S.; Lethesh, K. C.; Fiksdahl, A. Fuel oil desulfurization with dual functionalized imidazolium based ionic liquids. *Sep. Purif. Technol.* **2020**, *248*, 116959.
- (41) Li, S.-W.; Gao, R.-M.; Zhao, J.-s. Different supports of modified heteropolyacid for ultra-deep oxidative desulfurization: A newly easy shaped catalyst and the DFT cluster model study. *Fuel* **2019**, *237*, 840–850.
- (42) Li, Y.; Li, S.; Kong, Y. Hydroxylation of benzene to phenol over heteropoly acid $H_3PMo_{10}V_2O_{40}$ supported on amine-functionalized MCM-41. *RSC Adv.* **2021**, *11*, 26571–26580.
- (43) Liu, L.; Guo, F.; Xu, J.; Hu, J.; Wang, H.; Liu, H.; Wang, M. Adsorption-enhanced oxidative desulfurization by a task-specific pyridinium-based porous ionic polymer. *Fuel* **2019**, *244*, 439–446.
- (44) Na, C. K.; Park, G.-Y.; Park, H. Polypropylene surface with antibacterial property by photografting 1-vinylimidazole and subsequent chemical modification. *Korean J. Chem. Eng.* **2018**, *35*, 1748–1755.
- (45) Yang, H.; Jiang, B.; Sun, Y.; Zhang, L.; Sun, Z.; Wang, J.; Tantai, X. Polymer cation and isopolyanion ionic self-assembly: Novel thin-layer mesoporous catalyst for oxidative desulfurization. *Chem. Eng. J.* **2017**, *317*, 32–41.
- (46) Chen, Y.; Song, H.-y.; Lu, Y.-z.; Meng, H.; Li, C.-x.; Lei, Z.-g.; Chen, B.-h. Unified Catalytic Oxidation–Adsorption Desulfurization Process Using Cumene Hydroperoxide as Oxidant and Vanadate Based Polyionic Liquid as Catalyst and Sorbent. *Ind. Eng. Chem. Res.* **2016**, *55*, 10394–10403.
- (47) Liu, D.; Quek, X.-Y.; Hu, S.; Li, L.; Lim, H. M.; Yang, Y. Mesoporous TUD-1 supported molybdophosphoric acid (HPMo/TUD-1) catalysts for n-heptane hydroisomerization. *Catal. Today* **2009**, *147*, S51–S57.
- (48) John Xavier, R.; Dinesh, P. A study of the molecular, vibrational, electronic and quantum chemical investigation of 2-methyl-1-vinylimidazole. *Spectrochim. Acta, Part A* **2015**, *136*, 1569–1581.
- (49) Wolfart, F.; Hryniewicz, B. M.; Marchesi, L. F.; Orth, E. S.; Dubal, D. P.; Gómez-Romero, P.; Vidotti, M. Direct electrodeposition of imidazole modified poly(pyrrole) copolymers: synthesis, characterization and supercapacitive properties. *Electrochim. Acta* **2017**, *243*, 260–269.
- (50) Dizaji, A. K.; Mokhtarani, B.; Mortaheb, H. R. Deep and fast oxidative desulfurization of fuels using graphene oxide-based phosphotungstic acid catalysts. *Fuel* **2019**, *236*, 717–729.
- (51) Yu, Z.; Chen, X.; Zhang, Y.; Tu, H.; Pan, P.; Li, S.; Han, Y.; Piao, M.; Hu, J.; Shi, F.; et al. Phosphotungstic acid and propylsulfonic acid bifunctionalized ordered mesoporous silica: A highly efficient and reusable catalysts for esterification of oleic acid. *Chem. Eng. J.* **2022**, *430*, 133059.
- (52) Yu, L.; Liu, Q.; Ding, S.; Yu, J.; Peng, S.; Zhang, J.; Jiang, C.; Yang, G. The assembly of polyoxometalate-graphene oxide composites for photocatalytic removal of organic dye in water. *Appl. Surf. Sci.* **2022**, *602*, 154095.
- (53) Castanheiro, J. E.; Fonseca, I. M.; Ramos, A. M.; Vital, J. Tungstophosphoric acid immobilised in SBA-15 as an efficient heterogeneous acid catalyst for the conversion of terpenes and free fatty acids. *Microporous Mesoporous Mater.* **2017**, *249*, 16–24.
- (54) Gao, Y.; Gao, R.; Zhang, G.; Zheng, Y.; Zhao, J. Oxidative desulfurization of model fuel in the presence of molecular oxygen over polyoxometalate based catalysts supported on carbon nanotubes. *Fuel* **2018**, *224*, 261–270.
- (55) Hu, X.-M.; Chen, Q.; Zhao, Y.-C.; Laursen, B. W.; Han, B.-H. Facile synthesis of hierarchical triazine-based porous carbons for hydrogen storage. *Microporous Mesoporous Mater.* **2016**, *224*, 129–134.
- (56) Leng, Y.; Jiang, P.; Wang, J. A novel Brønsted acidic heteropolyanion-based polymeric hybrid catalyst for esterification. *Catal. Commun.* **2012**, *25*, 41–44.
- (57) He, J.; Wu, P.; Chen, L.; Li, H.; Hua, M.; Lu, L.; Wei, Y.; Chao, Y.; Zhou, S.; Zhu, W.; et al. Dynamically-generated TiO_2 active site on MXene Ti_3C_2 : Boosting reactive desulfurization. *Chem. Eng. J.* **2021**, *416*, 129022.
- (58) Yang, Y.; You, Y.; Wu, J.; Feng, J.; Zhang, Y. Phosphotungstic acid encapsulated in USY zeolite as catalysts for the synthesis of cyclohexylbenzene. *J. Iran. Chem. Soc.* **2020**, *18*, 573–580.
- (59) Wang, H.; Wang, C.; Zhao, M.; Yang, Y.; Fang, L.; Wang, Y. $H_3PMo_{10}V_2O_{40}$ anchor by OH of the Titania nanotubes: Highly efficient heterogeneous catalyst for the direct hydroxylation of benzene. *Chem. Eng. Sci.* **2018**, *177*, 399–409.
- (60) Silversmit, G.; Depla, D.; Poelman, H.; Marin, G. B.; De Gryse, R. Determination of the V2p XPS binding energies for different vanadium oxidation states (V^{5+} to V^{0+}). *J. Electron Spectrosc. Relat. Phenom.* **2004**, *135*, 167–175.
- (61) Wang, C.; Chen, Z.; Yao, X.; Jiang, W.; Zhang, M.; Li, H.; Liu, H.; Zhu, W.; Li, H. One-pot extraction and aerobic oxidative desulfurization with highly dispersed V_2O_5 /SBA-15 catalyst in ionic liquids. *RSC Adv.* **2017**, *7*, 39383–39390.
- (62) Zhu, Z.; Lin, H.; Chi, M.; Gao, X.; Feng, Y.; Yang, K.; Lü, H. Unveiling structure-function relationships in deep eutectic solvents based biomimetic catalysis for aerobic oxidative desulfurization. *Fuel* **2022**, *308*, 122070.
- (63) Yang, H.; Luo, M.; Lu, S.; Zhang, Q.; Chao, Y.; Lv, F.; Zhu, L.; Bai, L.; Yang, L.; Wang, W.; et al. Low-temperature aerobic oxidation of thiophenic sulfides over atomic Mo hosted by cobalt hydroxide sub-nanometer sheets. *Chem* **2022**, *8*, 2460–2471.